Enabling Superprotonic Phase Transitions in Solid Acids via Supramolecular Complex Formation: The Case of Crown Ethers and Alkali Hydrogen Sulfates

Enabling Superprotonic Phase Transitions in Solid Acids Via Supramolecular Complex Formation: The Case of Crown Ethers and Alkali Hydrogensulfates

Samet Ocak,[a] Simone d'Agostino,[a] Grega Venturini,[a] Francesca Soavi,[a]* Simone Bordignon,[b] Michele R. Chierotti,[b]* and Dario Braga[a]*

[a] Department of Chemistry "Giacomo Ciamician", Alma Mater Studiorum Università di Bologna, Via F. Selmi, 2, 40126 Bologna, Italy.

[b] Dipartimento di Chimica and NIS Centre, University of Torino, Via P. Giuria, 7, 10125 Torino, Italy

AUTHOR INFORMATION

Corresponding Author

* (S. D.) E-mail: simone.dagostino2@unibo.it.

* (M. R.C.) E-mail: michele.chierotti@unito.it.

* (F. S.) E-mail: fracesca.soavi@unibo.it.

ABSTRACT

This investigation, combining both structural and spectroscopic analyses, sheds light on the intricate relationship between conduction properties and the initiation of dynamic motions within the anhydrous crystalline materials of 18-crown-6·KHSO4 (1) and 18-crown-6·RbHSO4 (2), and prove how the formation of supramolecular complexes is pivotal for inducing solid-solid transitions, leading to superprotonic phases, i.e., crystalline solids exhibiting an enhanced ability to conduct protons, as elucidated through impedance spectroscopic measurements. This multifaceted approach deepens our understanding of the phenomenon and sets the stage for further exploration and application in solid-state protonic conductors.

TOC GRAPHICS

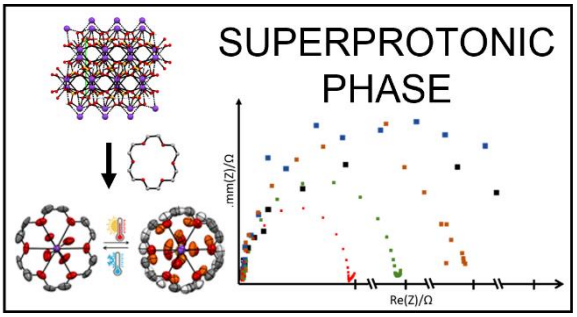

INTRODUCTION

The design and development of solid electrolytes, i.e., materials displaying fast ion conduction features, have received great attention over the last decades for applications in many electric devices such as molecular sensors, supercapacitors, batteries, and fuel cells.[1–8] One notable example is Nafion, an organic polymer with sulfonic acid residues that is reported to display conductivity within the range 10^{-1}–10^{-5} S cm^{-1} that is highly depending on temperature, hydration state, thermal history and processing conditions.[9–15] Therefore, materials with good proton conductivity at a higher temperature range (100–300 °C) under dry or anhydrous conditions are particularly sought.[7,16–19] Many alternatives have been proposed so far, e.g., polymers, Metal Organic Frameworks (MOFs) and Covalent Organic Frameworks (COFs), metal oxides, glasses, and Plastic Crystals (PCs) have shown promising features for proton conductivity.[5,11,16,18,20–30] Solid acids with formula $MHAO_4$ and MH_2BO_4 (where M = alkali cation, A = S, Se; B = P, As) have also been shown to possess elevated protonic conductivity due to the existence of dynamically disordered hydrogen-bond networks associated with the onset of reversible, first order, solid-solid transitions, named superprotonic phase transitions.[2,31–34] It has also been shown that proton conductivity is higher in presence of larger cations, e.g., Cs^+ versus Rb^+ and K^+.[33,35] For instance, $CsHSO_4$, among the alkali series, is the only one that shows the superprotonic phase transition from monoclinic to tetragonal at 142 °C.[36,37] When the cation size decreases on passing from Cs^+ (0.170 nm) to Rb^+ (0.149 nm) and K^+ (0.138 nm)[38] the transition is no longer observed,[39] which makes the potassium and rubidium hydrogen sulfate salts not useful as solid proton electrolytes.[40]

Crown ethers have been extensively studied in the past decades for their ability to coordinate alkali and various metal ions.[41–46] Many studies on alkali metal cations coordinated to the crown ethers show how these supramolecular complexes are prone to undergoing one or more solid-solid phase transitions that may present dynamic features.[43,47–49] It has also been pointed out that the cation that

is selectively captured in the crown ethers' cavities has an explicit effect on the dynamics of these complexes.[56,57] The anhydrous supramolecular complex made up of 18-crown-6 and potassium hydrogen sulfate, 18-crown-6·$KHSO_4$ (**1**), was reported to undergo an enantiotropic solid-solid transition, which was believed, but never proved, to be associated with the onset of a dynamical process affecting the crown ether ligand and/or the hydrogen sulfate anion.[49]

After almost 20 years, we finally give insights into the genuine nature of such a transition, which leads to a superprotonic phase. To this end we have prepared fresh samples of dihydrate 18-crown-6·$KHSO_4$·$2H_2O$ (**1**·$2H_2O$) and 18-crown-6·$RbHSO_4$·$2H_2O$ (**2**·$2H_2O$) (Figure S-1) that transform into their anhydrous phases **1** (Figure S-2) and **2** by being heated up to 70 °C. On further heating, they both undergo phase transitions to a superprotonic phase, which reverts to an ordered structure on cooling. Then, we studied their proton conduction features by means of Electrochemical Impedance Spectroscopy (EIS) in an anhydrous environment while investigating the phase transitions by Differential Scanning Calorimetry (DSC). In terms of proton conductivity, the anhydrous rubidium supramolecular salt displays significantly better conduction features compared to the potassium one already at room temperature (RT) and at high temperature (HT) as well. In addition, Variable-Temperature XRD and solid-state NMR (SSNMR) spectroscopy have been used to shed light and elucidate the conducting behavior in relation to the structural and dynamic features of these supramolecular compounds.

METHODS

Synthesis. The supramolecular complex salt of 18-crown-6·$KHSO_4$ (**1**) was prepared according to the literature[49] and its structure was redetermined, whereas 18-crown-6·$RbHSO_4$·$2H_2O$ (**2**·$2H_2O$) was obtained by dissolving 100 mg (0.38 mmol) of 18-crown-6 (from Tokyo Chemical Industries, > 98%)

and 69 mg (0.38 mmol) of $RbHSO_4$ in a beaker filled with ca. 3 mL of water, and the resulting solution was left to slowly evaporate affording single crystal specimens suitable for XRD analysis. The anhydrous crystals of **1** and **2** were prepared by dissolving the starting materials in a beaker filled with ca. 10 mL of dry acetone, left in a desiccator for crystallization by slow evaporation; alternatively, powders of anhydrous **2** could be prepared by heating a sample of **2**·$2H_2O$ at 80 °C overnight. $RbHSO_4$ was synthesized starting from Rb_2SO_4 (Sigma-Aldrich 99.8%): once dissolved in water, an excess amount of H_2SO_4 (Sigma-Aldrich 95.0-98.0%) was added to solution and left to evaporate. After few days, large crystals were obtained, vacuum-dried, rinsed quickly with water and acetone and finally placed in an oven at 80 °C for 12 h to dry.

X-Ray diffraction (XRD). Single-crystal data for 18-crown-6·$KHSO_4$ and 18-crown-6·$RbHSO_4$·$2H_2O$ (**2**·$2H_2O$) at RT and for 18-crown-6·$RbHSO_4$ (**2**) at RT and –170 °C were collected on an Oxford X'Calibur S CCD diffractometer equipped with a graphite monochromator (Mo-Kα radiation, λ = 0.71073 Å), and an Oxford CryoStream800 cryostat. In each case, crystals showed twinning, and the reflection data were integrated with the default configuration for twinned crystals of the CrysAlisPro Software. Subsequent structural solution and refinement were performed using the HKLF4 file containing non-overlapped reflections. Data for 18-crown-6·$KHSO_4$ (**1**) at 90 °C were collected at Single Crystal XRD1 beamline of the Elettra synchrotron radiation facility. An air blower was used to allow high-temperature data collection and the X-ray wavelength was set to 0.7 Å. The data was integrated by the XDS program.[50,51]

The structures were solved with SHELXT[52] by intrinsic phasing and refined on F^2 with SHELXL[53] implemented in the Olex2 software[54] by full-matrix least squares refinement. H_{OH} atoms were either directly located or, when not possible, added in calculated positions; H_{CH} atoms for all compounds were added in calculated positions and refined riding on their respective carbon atoms. All non-

hydrogen atoms were anisotropically refined and the rigid-body RIGU restraints applied.[53] Crystal structures of **1** at 90 °C, **2**·2H_2O, and **2** exhibited crystallographic disorder. In **1**, both the 18-crown-6 and the HSO_4^- anion were treated as disordered over two positions, the site occupancy factors (SOFs) were refined by adding a second free variable in the FVAR command line. SOFs for the two positions of the crown ether and anion were refined to 0.7 and 0.3, while the sulfate anion displayed occupancies of 0.6 and 0.4. In **2**·2H_2O, the anion was also disordered over two positions with SOFs refined to 0.4 and 0.6. In **2** at RT, the sulfate anion was treated as disorder over three positions and SOFs were refined to values of 0.4, 0.4, and 0.2, respectively. Data collection and refinement details are listed in Table S-1. The Mercury[55] program was used for molecular graphics and calculation of intermolecular interactions. Crystal data can be obtained free of charge via www.ccdc.cam.ac.uk/conts/retrieving.html (or from the Cambridge Crystallographic Data Centre, 12 Union Road, Cambridge CB21EZ, UK; fax: (+44)1223-336-033; or e-mail: deposit@ccdc.cam.ac.uk); CCDC numbers 2309182-2309186.

For phase identification and variable-temperature purposes, powder X-ray diffractograms were collected, in the 2θ range 5–40°, on a Panalytical X'Pert PRO automated diffractometer equipped with an X'Celerator detector and in Bragg-Brentano geometry and using Cu Kα radiation without a monochromator (step size = 0.02°; time/step = 20 s; 0.04 rad soller; 40mA x 40kV). The program Mercury[55] was used to calculate the powder X-ray patterns based on single-crystal data collected in this work or retrieved from the ICSD or CCDC. In all cases, the identity between polycrystalline samples and single crystals was always verified by comparing experimental and calculated powder diffraction patterns (see below).

Differential Scanning Calorimetry. DSC measurements were performed with a PerkinElmer DSC-7 equipped with a PII intracooler. Temperature and enthalpy calibrations were performed using high-

purity standards (*n*-decane, benzene, and indium). Heating of the aluminum pan containing the sample (3–5 mg) was carried out at 5 °C min^{-1} in the temperature range 30–130 °C under N_2 atmosphere. Entropy change was estimated by dividing the enthalpy change by the transition temperature.

Thermogravimetric Analysis. TGA was performed with a PerkinElmer TGA-7. The samples were contained in a platinum crucible and heated to 300 °C at a rate of 5 K min^{-1} under nitrogen flow (20 cm^3 min^{-1}). Sample weights were in the range of 1.5–5 mg.

Hot stage and cross-polarized optical microscopy HSM-CP experiments were carried out using a Linkam TMS94 device connected to a Linkam LTS350 platinum plate and equipped with polarizing filters. Images were collected with a NIKON DS FI3 camera, from an Olympus BX41 stereomicroscope.

Electrochemical Impedance Spectroscopy (EIS). Ionic conductivity was measured by electrochemical impedance spectroscopy on 13 mm-diameter pellets, featuring thicknesses of 0.81 mm for **2**, and 0.9 mm for **1** pressed at 10 tons for 5 min and coated with silver paint. To exclude any contribution from humidity to the sample ionic conductivity, before measurements, the pellets were dried at 80 °C under vacuum oven for 12 h (Büchi glass oven B-585), and then transferred into a dry box (Ar atmosphere, H_2O, and O_2 < 1 ppm, MBraun) for cell assembly and test. The pellets were placed between two stainless steel blocking electrodes (1.6 cm-diameter) housed in a two electrode, Swagelok-type cell. The EIS spectra were collected by a VSP multichannel potentiostat/galvanostat/FRA (BioLogic, Seyssinet-Pariset, France) within 700 kHz–10 mHz frequency range and with an AC perturbation of 25 mV, acquiring 5 points per decade. The cells were

thermostated at different temperatures (from 25 to 150 °C) by a Büchi glass oven B-585 placed inside the dry box. Samples were thermostated for 30 min before every measurement. The EIS Nyquist plots were fitted using the EC-LAB software. Conductivity (σ) was calculated according to the following equation:

$$\sigma = \frac{1}{\rho} = \frac{L}{A\,R} \qquad (1)$$

Where ρ is the resistivity, A is the pellet cross sectional area, R is the total resistance (evaluated by EIS), L is the pellet thickness.

Arrhenius plots are drawn in order to calculate the activation energies before and after the phase transition regions by using the Arrhenius equation:

$$\sigma(T) = \frac{\sigma_0}{T} \exp\left(-\frac{E_a}{k_b \cdot T}\right) \qquad (2)$$

Where σ_0 is a pre-exponential constant and E_a is the activation energy, k_b is the Boltzmann constant, and T is the temperature.

Solid-state NMR (SSNMR). ^{1}H MAS experiments were run on a Jeol ECZR 600 instrument, operating at a frequency of 600.13 MHz for ^{1}H and equipped with a 3.2 mm probe. A 3.2 mm zirconia rotor (o.d. = 60 μL) specific for high-temperature analyses was packed with an appropriate amount of **1** or **2**, previously kept in an oven at 80 °C for 3 h to ensure complete anhydrification. The ^{1}H MAS spectra were acquired with the DEPTH sequence (π/2–π–π) for the suppression of the probe background signal at different temperatures (reported in Table S-3) at a spinning speed of 18 kHz (^{1}H 90° = 2.0 μs; 16 scans; optimized relaxation delays ranging from 3 to 90 s, depending on the sample and on the temperature). ^{1}H T_1 values were measured for the 4.0 ppm signal relative to the crown ether by means of ^{1}H SSNMR saturation recovery: at the different temperatures, 12 ^{1}H spectra were acquired for 1 scan with different relaxation delays, included in the range 0.1–200 s and calculated

by the Delta v5.2.1 software through an exponential algorithm. The ^{1}H chemical shift scale was calibrated with adamantane (^{1}H signal at 1.87 ppm with respect to primary standard tetramethylsilane) as an external standard. Temperature calibration on this probe was performed by acquiring ^{207}Pb MAS spectra on external standard $Pb(NO_3)_2$.

RESULTS AND DISCUSSION

The supramolecular complexes **1**, **2**, **1**·$2H_2O$, and **2**·$2H_2O$ were synthesized, according to the literature,[49] by simply mixing equimolar amounts of $KHSO_4$ or $RbHSO_4$ with 18-crown-6 in water or dry acetone depending on the desired phase of the complex. In the case of **1,** a reversible solid-solid transition takes place at ca. 120 °C leading to a high-temperature phase, denoted as **1-HT**. In the hydrated compound **2**·$2H_2O$, a first endothermic peak at 60 °C is observed, associated with water loss and formation of anhydrous **2** which, on further heating, shows two close peaks at 116 and 122 °C (Figure S1-4). These endothermic processes appear to be associated to two distinct solid-solid phase rearrangements leading to high-temperature phases, denoted as **2-HT'** and **2-HT**. Given the narrow difference in temperature between **2-HT'** and **2-HT,** the intermediate high-temperature phase **2-HT'** could not be isolated (Figures S-5, and S-8). The water loss from dehydration processes and thermal stabilities of the complexes were confirmed by TGA analyses (Figures S-6 and S-7).

Proton conductivity for **1** and **2** was investigated by EIS under dry conditions in the temperature range 22–150 °C starting from the anhydrous phases **1** and **2** to high-temperature phases **1-HT** and **2-HT** (Figure 1). Measurements were conducted in an Ar-filled glove box using the pellets of the samples placed between two stainless steel blocking electrodes housed in a two-electrode cell.

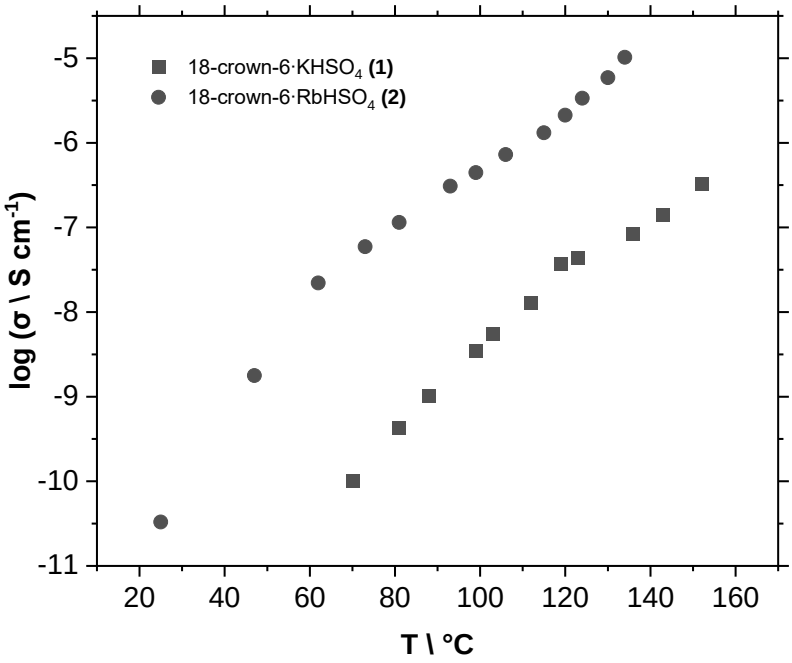

Figure 1. Trend of the ionic conductivity of **1** and **2** *vs* temperature.

For each tested temperature, the Nyquist plots (Figures S-9 and S-10) were analyzed according to the equivalent circuit reported in Figure S-11, which consists of the electronic resistance (R1) in series with the (R2/Q2) branch, where R2 stands for the bulk ionic resistance in parallel with Q2, that represents the double layer capacitance set at the two ionic conductor/electrode interfaces.[18]

Temperature-dependent conductivity plots are reported in Figure 1 for **1** and **2**. The supramolecular complexes share some similarities but also show differences which are intimately related to the crystal packing features. The rubidium complex performs better than the potassium one, i.e., at RT it features a conductivity of $3.3 \cdot 10^{-11}$ S cm^{-1} that is comparable to the conductivity of its potassium analogue at 70 °C.

At RT, **1** and **2** are almost isostructural (Table S-1) and single-crystal analysis shows that the alkali cations, K^+ and Rb^+, are coordinated by O-atoms from the 18-crown-6 and sulfates, each complex

self-assembling into dimers held by hydrogen-bonded HSO_4^- anionic pairs (Figure 2 and Table S-2). The dimers are packed in such a way as to form sections where these HSO_4^- anionic pairs are hosted, as shown in Figure 2. The sections run parallel to the crystallographic *a*- or *b*-axis for **1** and **2**, respectively, and possess an internal diameter of ca. 11 Å. Close inspection reveals that the sulfate anions within crystalline **2** exhibit crystallographic disorder over several positions of the oxygen atoms, indicative that a dynamic process is taking place that is stopped only on cooling down to –170 °C (Supporting Information). The reordering occurs via a reversible phase transition from monoclinic $P2_1/n$ to triclinic $P\bar{1}$ (Table S-1). Interestingly, the dynamic process, a "swinging" of the sulfates between the multiple positions, is associated with the improved ionic conductivity behavior of the complex. Furthermore, the unit cell of **2** is not as efficiently packed as in **1**, which indicates the existence of free space that facilitates the proton diffusion through the structure.

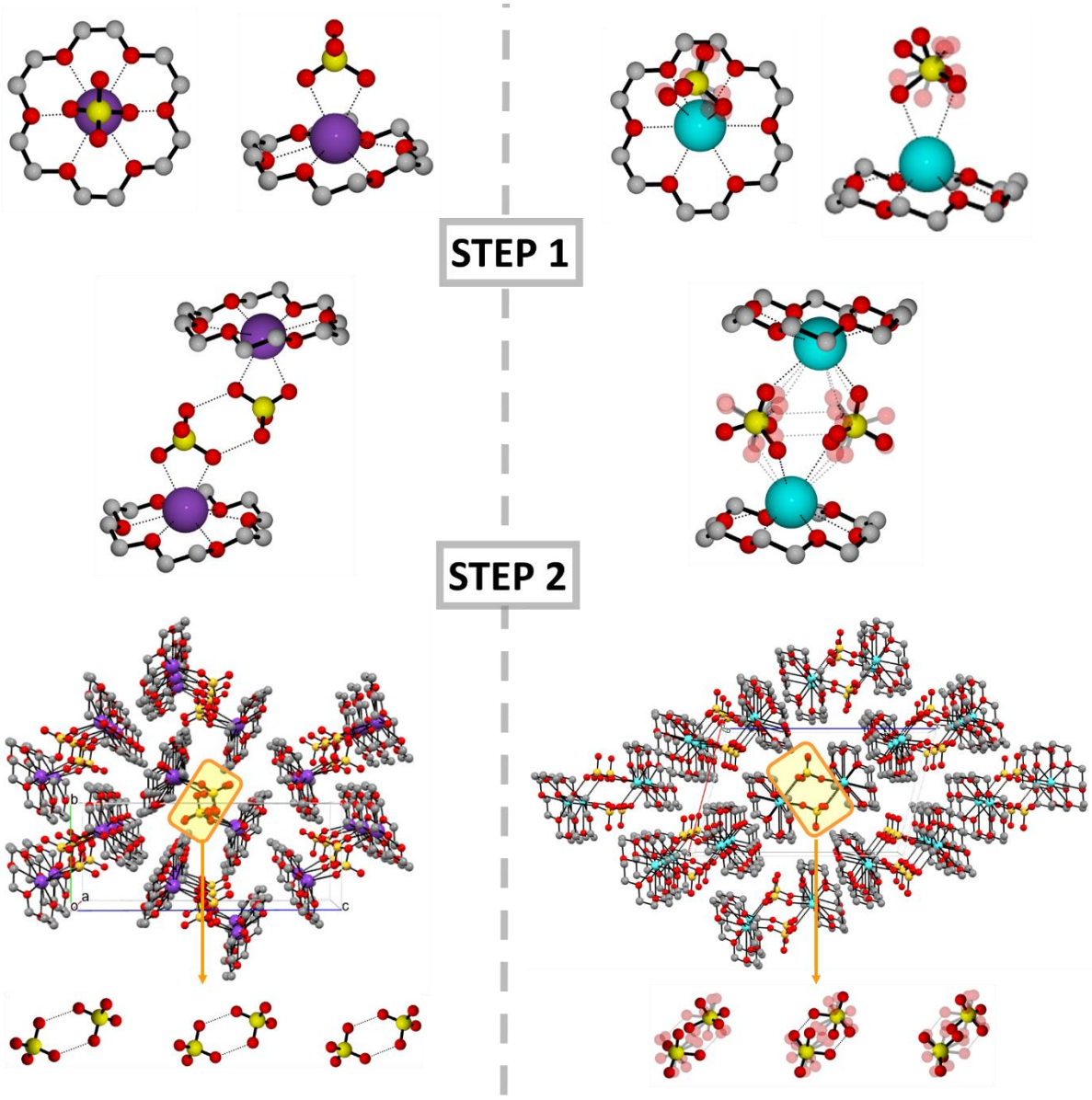

Figure 2. Hierarchical self-assembly of **1** (left) and **2** (right) from the complexes to the supramolecular units (step 1) and crystal packing (step 2); a detail of the HSO_4^- anions hosted within the section channel is also given at the bottom. Note that the disorder of the HSO_4^-affecting **2** is depicted with transparency. H atoms omitted for clarity.

For **1**, the conductivity reaches the measurable range at 70 °C ($1.01 \cdot 10^{-10}$ S cm^{-1}). Increasing the temperature up to 112 °C, right before phase transition, it accounts for $1.26 \cdot 10^{-8}$ S cm^{-1} with an

activation energy (E_a) of 133.96 ± 2.93 kJ mol^{-1} (see Arrhenius plots reported in Figure S-12 in the Supporting Information). As it can be seen from Figure 1, the conductivity "jumps" by further increasing the temperature. Above the phase transition temperature, **1-HT** reaches the value of $3.24 \cdot 10^{-7}$ S cm^{-1} at 152 °C with an E_a of 91.12 ± 9.14 kJ mol^{-1}. In the case of **2**, a sharp increase of conductivity with an E_a of 148.3 ± 1.66 kJ mol^{-1} was observed from RT to 60 °C which is likely associated with a sharp increase of the structural disorder. On further increasing the temperature, the conductivity increases to $7.26 \cdot 10^{-7}$ S cm^{-1} up to the phase transition range with an E_a of 86.96 ± 0.98 kJ mol^{-1}. After phase transition, the conductivity reaches $1.02 \cdot 10^{-5}$ S cm^{-1} at 134 °C with an E_a of 143.13 ± 5.72 kJ mol^{-1}.

It is worth noting that the pure solid acids $KHSO_4$ and $RbHSO_4$, which do not undergo any phase transition, do not show any such variation.[39,58]

These features are likely related to the increasing dynamic motions of the 18-crown-6 molecules and sulfates with temperature. Even though, as shown above, at RT compound **1** displays an ordered structure, as the temperature is raised to just before the phase transition (90 °C), according to the data collected in synchrotron radiation facility Elettra, the complex undergoes disordering of the components. Distinct split positions for the 18-crown-6 and HSO_4^- atoms could be easily identified from the electron density map and were treated accordingly. The marked tangential elongation of the thermal ellipsoids (Figures S-1 and S-2) clearly indicates the preferential direction of the reorientational process.

Unfortunately, the rearrangement associated with the transition from **1** to **1-HT** leads to crystal crumbling (Figure S-5c). Analogously, in the case of **2** the transition to **2-HT** also leads to crystal disruption; moreover, the exceptionally high degree of disorder affecting the crown ether and sulfate prevented the modeling of the structure of **2** also at 90 °C (Figure S-5a).

Altogether, these data confirm the high degree of structural flexibility of the crown ether complex, with two simultaneous dynamic processes, namely the reorientation of the crown ether and of the sulfates, as the temperature is increased before the transition point. Above transition, **1** and **2** undergo a significant rearrangement to **1-HT** and **2-HT**, which are likely dynamically disordered phases.

The analysis of relaxation parameters (T_1, T_2 and $T_{1\rho}$), in SSNMR [59,60] is a well-established tool to investigate the dynamics of the system over a large temporal scale (from ps to h).[61] In the case of hydrogen-containing materials, the analysis of the ^1H T_1 is the most favourable, due to ^1H being the most NMR-active nucleus with high natural abundance.

Regarding compounds **1** and **2**, the ^1H T_1 relaxation times were measured by ^1H MAS (18 kHz) SSNMR saturation recovery at variable temperatures (reported in Table S-3 in the Supporting Information). The complete ^1H MAS SSNMR spectra are reported in Figure S-13 in the Supporting Information. For both **1** and **2**, the crown ether resonance (at 4.0 ppm), accounting for 12 protons, apparently consists of at least two entangled contributions; it becomes narrower and narrower with raising T, which indicates an expected increase in the mobility of the moiety. On the other hand, two peaks at higher frequencies (11.4 and 12.2 ppm, for **1** and **2**, respectively), ascribable to the hydrogen sulfate proton, do not change their width significantly; nonetheless, a slight variation in their chemical shifts is observed in both cases when T is increased. Specifically, the HSO_4^- of **1** undergoes an overall shift towards lower frequencies of 0.2 ppm throughout the whole range of temperature; that of **2** moves to higher ppm, up to 12.4 ppm at the highest temperature. Unfortunately, the ^1H signals relative to the mobile HSO_4^- protons were in any case too little intense to provide reliable T_1 values. Thus, the results of this specific analysis cannot supply insight into the ionic conductivity of these systems, intrinsic in the mobile hydrogen sulfate proton. Therefore, the study of the ^1H relaxation times for **1** and **2** (see Figure 3 below) was focused solely on the crown ether signal. The figure shows the resulting plots between the natural logarithm of the measured ^1H T_1 values and the inverse of the

corresponding absolute temperatures for **1** and **2**. For both compounds, the plots are associated only to the mobility of the 18-crown-6 moiety (peak at 4.0 ppm).

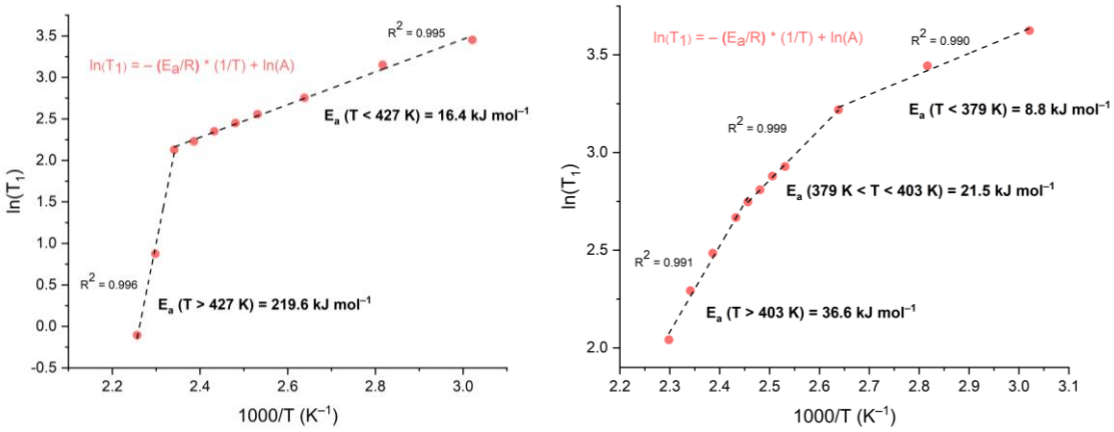

Figure 3. Temperature (K) dependence of ^{1}H spin-lattice relaxation time (T_1), peak at 4.0 ppm, for **1** (left) and **2** (right), in logarithmic scale (with respective general equation in red). The R^2 coefficients of determination for the different linear fits are reported, as well as the E_a values corresponding to the slopes of the linear fits.

By building logarithmic Arrhenius plots it is possible to detect variations in the slopes of the fitting lines, which indicate discrete motional regimes. The corresponding values of activation energy (E_a) provided by the Arrhenius law are thus extracted directly from the various observed slopes. In our study, the plot leads to deduce that for **1** two distinct motion regimes exist, one below ca. 154 °C (E_a = 16.4 ± 0.5 kJ mol^{-1}) and one over 154 °C (E_a = 219.6 ± 13.1 kJ mol^{-1}). As for **2**, three different dynamic behaviors can be assessed: one below 106 °C (E_a = 8.8 ± 0.9 kJ mol^{-1}), one between 106 and 130 °C (E_a = 21.5 ± 0.4 kJ mol^{-1}) and one over 130 °C (E_a = 36.6 ± 2.0 kJ mol^{-1}).

It is worth noting that the transitions T and E_a values provided by SSNMR differ from those obtained by TGA and EIS analyses. This is because the three techniques are in principle observing different phenomena, *i.e.*, the rotation of the crown ether, the occurrence of the polymorphic transitions, and the mobility of the hydrogen sulfate proton. In general, these three phenomena may

or may not influence each other, and especially polymorphic transitions could induce an increased or decreased rotation of the crown ether. Moreover, the very nature of the considered aspects may be different: for example, the dynamics of crown ethers usually change in a continuous fashion when increasing the temperature, while the polymorphic transitions occur at discrete T ranges. In the case of our samples, the data suggests that the three phenomena are independent from each other.

CONCLUSIONS

The present study contributes to the design of novel supramolecular solids and paves the way to the exploitation of crown ether complex formation to enable superprotonic phase transitions in solid acids, which otherwise would not be accessible. The supramolecular complexes 18-crown-6·$KHSO_4$ (**1**) and 18-crown-6·$RbHSO_4$ (**2**) have been synthesized and characterized; in each case, ion transport increases by several orders of magnitude upon the phase transition. The combined structural and spectroscopic study illustrates how conductivity features are associated with the onset of dynamical processes affecting the crown ether ligand and the hydrogen sulfate anion, already before the phase transition; thus, this demonstrates, as a proof of concept, that supramolecular complex formation between crown ethers and alkali hydrogen sulfates indeed enables superprotonic phase transitions promoted by temperature increase, which otherwise would not be accessible. Work is ongoing to test other combinations of alkali metal cations, anions (HSO_4^- and $HSeO_4^-$), and crown ethers, as well as the possibility of attaining crystalline solid solutions[62,63] for the fine-tuning of the temperatures and performances of superprotonic phase transitions.

ASSOCIATED CONTENT

Supporting Information is available free of charge via the Internet at http://pubs.acs.org. Additional information concerning experimental procedure, PXRD, crystal data and refinement details, DSC and TGA traces, CP-HSM images, Electrochemical Impedance Spectroscopy, and Arrhenius Plots, Solid-

state NMR results, X-ray crystallographic data (CIF files) for 1 at RT, 1 at 90 °C, 2·2H2O, 2 at RT and 2 at –170 °C are available free of charge.

AUTHOR INFORMATION

Corresponding Authors

* (S. D.) E-mail: simone.dagostino2@unibo.it.

* (T. S.) E-mail: tommaso.salzillo@unibo.it.

* (F. S.) E-mail: fracesca.soavi@unibo.it.

Orcid and E-mail

Samet Ocak: 0000-0003-2649-0549; samet.ocak3@unibo.it

Simone d'Agostino: 0000-0003-3065-5860; simone.dagostino2@unibo.it

Grega Venturini: grega.venturini@studio.unibo.it

Francesca Soavi: 0000-0003-3415-6938; francesca.soavi@unibo.it

Simone Bordignon: simone.bordignon@unito.it

Michele Remo Chierotti: 0000-0002-8734-6009; michele.chierotti@unito.it

Dario Braga: 0000-0003-4162-4779; dario.braga@unibo.it

Author Contributions

The manuscript was written through contributions of all authors. All authors have given approval to the final version of the manuscript.

Notes

The authors declare no competing financial interest.

ACKNOWLEDGMENT

S.D. F.S. and D.B acknowledge the University of Bologna for financial support (RFO-scheme); S.D., and F.S. thank the Italian MUR (Fondi PNRR-CNMS-Spoke 13-MOST Code: CN00000023) for financial support.

REFERENCES

(1) Hilczer, B.; Pawlaczyk, C.; Salman, F. E. Superionic Phase Transition In CsHSe04 And CsDSe04 Single Crystal. *Ferroelectrics* **1988**, *81*, 193–196.

(2) Boysen, D. A.; Uda, T.; Chisholm, C. R. I.; Haile, S. M. High-Performance Solid Acid Fuel Cells Through Humidity Stabilization. *Science* **2004**, *303*, 68–70.

(3) Haile S. M.; Kreuer K. D.; Maier J. Structure of $Cs_3(HSO4)_2(H_2PO_4)$ - a New Compound with a Superprotonic Phase Transition. *Acta. Crystallogr. B.* **1995**, *B51*, 680–687.

(4) Sinitsyn, V. V; Baranov, A. I.; Ponyatovsky, E. G. Pressure Effect on Superprotonic Phase Transition in Mixed $[(NH_4)_xRb_{1-x}]_3H(SO_4)_2$ Crystals. *Solid State Ion.* **2000**, *136-137*, 167-171.

(5) Wang, L. S.; Patel, S. V.; Sanghvi, S. S.; Hu, Y. Y.; Haile, S. M. Structure and Properties of $Cs_7(H_4PO_4)(H_2PO_4)_8$: A New Superprotonic Solid Acid Featuring the Unusual Polycation $(H_4PO_4)^+$. *J. Am. Chem. Soc.* **2020**, *142*, 19992–20001.

(6) Fan, L.; Tu, Z.; Chan, S. H. Recent Development of Hydrogen and Fuel Cell Technologies: A Review. *Energy Rep*. **2021**, *7*, 8421–8446.

(7) Zeng, M.; Liu, W.; Guo, H.; Li, T.; Li, Q.; Zhao, C.; Li, X.; Li, H. Polyoxometalate-Cross-Linked Proton Exchange Membranes with Post-Assembled Nanostructures for High-Temperature Proton Conduction. *ACS Appl. Energy Mater.* **2022**, *5*, 9058–9069.

(8) Tang, H.; Li, J.; Wang, Z.; Zhang, H.; Pan, M.; Jiang, S. P. Self-Assembly of Nanostructured Proton Exchange Membranes for Fuel Cells. *ACS Symp. Ser. Am. Chem. Soc.* **2013**, *1140*, 243–263.

(9) Kusoglu, A.; Weber, A. Z. New Insights into Perfluorinated Sulfonic-Acid Ionomers. *Chem. Rev.* **2017**, *117*, 987–1104.

(10) Sonef, Y.; Ekdunge, P.; Simonsson, D. Proton Conductivity of Nafion 117 as Measured by a Four-Electrode AC Impedance Method. *J. Electrochem. Soc.* **1996**, *143*, 1254-1259.

(11) Gao, H.; Lian, K. Proton-Conducting Polymer Electrolytes and Their Applications in Solid Supercapacitors: A Review. *RSC Adv*. **2014**, *4*, 33091–33113.

(12) Yamada, T.; Sadakiyo, M.; Kitagawa, H. High Proton Conductivity of One-Dimensional Ferrous Oxalate Dihydrate. *J. Am. Chem. Soc.* **2009**, *131*, 3144–3145.

(13) Schuster, M.; Meyer, W. H.; Wegner, G.; Herz, H. G.; Ise, M.; Kreuer, K. D.; Maier, J. Proton Mobility in Oligomer-Bound Proton Solvents: Imidazole Immobilization via Flexible Spacers. *Solid State Ion.* **2001**; *145*, 85-92.

(14) Li, G. H.; Lee, C. H.; Lee, Y. M.; Cho, C. G. Preparation of Poly(Vinyl Phosphate-b-Styrene) Copolymers and Its Blend with PPO as Proton Exchange Membrane for DMFC Applications. *Solid State Ion.* **2006**, *177*, 1083–1090.

(15) Karadedeli, B.; Bozkurt, A.; Baykal, A. Proton Conduction in Adipic Acid/Benzimidazole Hybrid Electrolytes. *Physica. B. Condens. Matter* **2005**, *364*, 279–284.

(16) Jhariat, P.; Kumari, P.; Panda, T. Structural Features of Proton-Conducting Metal Organic and Covalent Organic Frameworks. *CrystEngComm* **2020**, *22*, 6425–6443.

(17) Kajita, T.; Tanaka, H.; Ohtsuka, Y.; Orido, T.; Takano, A.; Iwamoto, H.; Mufundirwa, A.; Imai, H.; Noro, A. Effects of a Nanophase-Separated Structure on Mechanical Properties and Proton Conductivity of Acid-Infiltrated Block Polymer Electrolyte Membranes under Non-Humidification. *ACS Omega* **2022**, *8*, 1121-1130.

(18) Ocak, S.; Poli, F.; Braga, D.; Salzillo, T.; Tarterini, F.; Carì, G.; Venuti, E.; Soavi, F.; d'Agostino, S. Design of Novel Solid-State Electrolytes Based on Plastic Crystals of Quinuclidinolium Methanesulfonate for Proton Conduction. *Cryst. Growth. Des.* **2023**, *23*, 4336–4345.

(19) Zheng, Z.; Li, M.; Zhou, Q.; Cai, L.; Yin, J. F.; Cao, Y.; Yin, P. Polyoxometalate-Poly(Ethylene Oxide) Nanocomposites for Flexible Anhydrous Solid-State Proton Conductors. *ACS Appl. Nano. Mater.* **2021**, *4*, 811–819.

(20) Rautenberg, M.; Bhattacharya, B.; Das, C.; Emmerling, F. Mechanochemical Synthesis of Phosphonate-Based Proton Conducting Metal-Organic Frameworks. *Inorg. Chem.* **2022**, *61*, 10801–10809.

(21) Ma, N.; Horike, N.; Lombardo, L.; Kosasang, S.; Kageyama, K.; Thanaphatkosol, C.; Kongpatpanich, K.; Otake, K. I.; Horike, S. Eutectic CsHSO4-Coordination Polymer Glasses with Superprotonic Conductivity. *J. Am. Chem. Soc.* **2022**, *144*, 18619–18628.

(22) Yang, Z.; Chen, P.; Hao, W.; Xie, Z.; Feng, Y.; Xing, G.; Chen, L. Sulfonated 2D Covalent Organic Frameworks for Efficient Proton Conduction. *Chem. Eur. J.* **2021**, *27*, 3817–3822.

(23) Enakieva, Y. Y.; Sinelshchikova, A. A.; Grigoriev, M. S.; Chernyshev, V. V.; Kovalenko, K. A.; Stenina, I. A.; Yaroslavtsev, A. B.; Gorbunova, Y. G.; Tsivadze, A. Y. Highly Proton-Conductive

Zinc Metal-Organic Framework Based On Nickel(II) Porphyrinylphosphonate. *Chem. Eur. J.* **2019**, *25*, 10552–10556.

(24) Meng, X.; Wang, H. N.; Song, S. Y.; Zhang, H. J. Proton-Conducting Crystalline Porous Materials. *Chem. Soc. Rev*. **2017**, *46*, 464–480.

(25) Caldes, M. T.; Kravchyk, K. V.; Benamira, M.; Besnard, N.; Gunes, V.; Bohnke, O.; Joubert, O. Metallic Nanoparticles and Proton Conductivity: Improving Proton Conductivity of BaCe0.9Y0.1O3-δ Using a Catalytic Approach. *Chem. Mater.* **2012**, *24*, 4641–4646.

(26) Winiarz, P.; Dzierzgowski, K.; Mielewczyk-Gryń, A.; Gazda, M.; Wachowski, S. High-Temperature Proton Conduction in LaSbO4. *Chem. Eur. J.* **2021**, *27*, 5393–5398.

(27) Ahn, S. M.; Park, J. E.; Jang, G. Y.; Jeong, H. Y.; Yu, D. M.; Jang, J. K.; Lee, J. C.; Cho, Y. H.; Kim, T. H. Highly Sulfonated Aromatic Graft Polymer with Very High Proton Conductivity and Low Hydrogen Permeability for Water Electrolysis. *ACS Energy Lett.* **2022**, *7*, 4427–4435.

(28) Scholz, T.; Schneider, C.; Terban, M. W.; Deng, Z.; Eger, R.; Etter, M.; Dinnebier, R. E.; Canepa, P.; Lotsch, B. V. Superionic Conduction in the Plastic Crystal Polymorph of Na4P2S6. *ACS Energy Lett.* **2022**, *7*, 1403–1411.

(29) Pal, S. C.; Mukherjee, D.; Sahoo, R.; Mondal, S.; Das, M. C. Proton-Conducting Hydrogen-Bonded Organic Frameworks. *ACS Energy Lett*. **2021**, *6*, 4431–4453.

(30) Sahoo, R.; Pal, S. C.; Das, M. C. Solid-State Proton Conduction Driven by Coordinated Water Molecules in Metal-Organic Frameworks and Coordination Polymers. *ACS Energy Lett.* **2022**, *7*, 4490–4500.

(31) Belushkint, A. V.; Carlile, C. J.; Shuvalov, L. A. A Quasielastic Neutron Scattering Study of Protonic Transport in Hydrogen-Bonded Alkali Metal Hydrogen Sulphates and Selenates. *Ferroelectrics* **1995**, *167*, 21–31.

(32) Belushkint, A. V; Carlilet, C. J.; ShuvalovO, L. A. The Diffusion of Protons in the Superionic Conductor $CsHSO_4$ by Quasielastic Neutron Scattering. *J. Phys. Condens. Matter* **1992**, *4*, 389-398.

(33) Friesel, M.; Baranowski, B.; Lunden, A. Pressure Dependence of the Transition to The Proton Conducting Phase of $CsHSO_4$, $CsHSeO_4$ and $RbHSeO_4$ Studied by Differential Scanning Calorimetry. *Solid State Ion*. **1989**, *35*, 85-89.

(34) Hassanzadeh Fard, Z.; Wong, N. E.; Malliakas, C. D.; Ramaswamy, P.; Taylor, J. M.; Otsubo, K.; Shimizu, G. K. H. Superprotonic Phase Change to a Robust Phosphonate Metal-Organic Framework. *Chem. Mater.* **2018**, *30*, 314–318.

(35) Kreuer K. D.; Dippel Th.; Hainovsky N. G.; Maier J. Proton Conductivity: Compounds and Their Structural and Chemical Peculiarities. *Ber. Bunsenges. Phys. Chem.* **1992**, *96*, 1736–1742.

(36) Kreuer, K. D.; Paddison, S. J.; Spohr, E.; Schuster, M. Transport in Proton Conductors for Fuel-Cell Applications: Simulations, Elementary Reactions, and Phenomenology. *Chem. Rev.* **2004**, *104*, 4637–4678.

(37) Kreuer, K. D. Fast Proton Conductivity: A Phenomenon between the Solid and the Liquid State?. *Solid State Ion.* **1997,** *94*, 55-62.

(38) Marcus, Y. Ionic Radii in Aqueous Solutions. *Chem. Rev.* **1988**, *88*, 1475-1498.

(39) Matsuda, A.; Oh, S. Y.; Nguyen, V. H.; Daiko, Y.; Kawamura, G.; Muto, H. Anhydrous Proton Conductivity of KHSO4-H3PW 12O40 Composites and the Correlation with Hydrogen Bonding Distance under Ambient Pressure. *Electrochim. Acta.* **2011**, *56*, 9364–9369.

(40) Baranov, A. I.; Fedosyuk, R. M.; Schagina, N. M.; Shuvalov, L. A. Structural Phase Transitions to the State with Anomalously High-Ionic Conductivity in Some Ferroelastic and Ferroelastic Crystals of the Bisulfate Group. *Ferroelectr. Lett. Sect.* **1984**, *2*, 25–28.

(41) Gokel, G. W.; Leevy, W. M.; Weber, M. E. Crown Ethers: Sensors for Ions and Molecular Scaffolds for Materials and Biological Models. *Chem. Rev.* **2004**, *104*, 2723–2750.

(42) Marczenko, K. M.; Mercier, H. P. A.; Schrobilgen, G. J. A Stable Crown Ether Complex with a Noble-Gas Compound. *Angew. Chem. Int.* **2018**, *130*, 12628–12632.

(43) Braga, D.; D'Agostino, S.; Grepioni, F.; Gandolfi, M.; Rubini, K. Crystal to Crystal Transformations and Polymorphism in Anionic Hydrogen Bonding Networks Stabilized by Crown Ether Metal Complexes. *Dalton Trans.* **2011**, *40*, 4765–4777.

(44) Braga, D.; D'Agostino, S.; Polito, M.; Rubini, K.; Grepioni, F. Caesium 18-Crown[6] Complexes with Aromatic Polycarboxylate Anions: Preparation, Solid-State Characterization and Thermal Behaviour. *CrystEngComm* **2009**, *11*, 1994–2002.

(45) Braga, D.; D'Agostino, S.; Grepioni, F. Surprising Robustness of a Unit Cell: Isomorphism in Caesium 18-Crown[6] Complexes with Aromatic Polycarboxylate Anions. *CrystEngComm* **2011**, *13* (5), 1366–1372.

(46) Yuan, G.-J.; Luan, Y.-T.; Miao, J.-B.; Wang, C.-F.; Chen, L.; Chen, C.; Chen, H.; Li, L.; Ren, X.-M. Crown-Ether-Ring Size Dependent Crystal Structures, Phase Transition and Dielectric

Properties of [M(Crown)]BF_4·xH_2O (M+=Na+, K+; Crown=15-Crown-5, 18-Crown-6; X=0 or 1). *Eur. J. Inorg. Chem.* **2023**, e202300523.

(47) Casimiro, A.; Lugger, J.; Lub, J.; Nijmeijer, K. Non-Globular Organic Ionic Plastic Crystal Containing a Crown-Ether Moiety – Tuning Its Behaviour Using Sodium Salts. *ChemPhysChem* **2022**, *23,* e202200258-e202200269.

(48) Braga, D.; Modena, E.; Polito, M.; Rubini, K.; Grepioni, F. Crystal Forms of Highly "Dynamic" 18-Crown[6] Complexes with M[HSO_4] and M[H_2PO_4] ($M^+ = NH_4^+$, Rb^+, Cs^+): Thermal Behaviour and Solid-State Preparation. *New J. Chem.* **2008**, *32*, 1718–1724.

(49) Braga, D.; Gandolfi, M.; Lusi, M.; Paolucci, D.; Polito, M.; Rubini, K.; Grepioni, F. Solution and Solid-State Preparation of 18-Crown[6] Complexes with M[HSO_4]n Salts ($M = NH_4^+$, K^+, Sr^{2+} and n = 1, 2) and an Investigation of Solvation/Desolvation Processes and Crystal Polymorphism. *Chem. Eur. J.* **2007**, *13*, 5249–5255.

(50) Kabsch, W. XDS. *Acta Crystallogr. D. Biol. Crystallogr.* **2010**, *66*, 125–132.

(51) Winn, M. D.; Ballard, C. C.; Cowtan, K. D.; Dodson, E. J.; Emsley, P.; Evans, P. R.; Keegan, R. M.; Krissinel, E. B.; Leslie, A. G. W.; McCoy, A.; McNicholas, S. J.; Murshudov, G. N.; Pannu, N. S.; Potterton, E. A.; Powell, H. R.; Read, R. J.; Vagin, A.; Wilson, K. S. Overview of the CCP4 Suite and Current Developments. *Acta Crystallogr. D: Biol. Crystallogr*. **2011**, *D67*, 235–242.

(52) Sheldrick, G. M. SHELXT - Integrated Space-Group and Crystal-Structure Determination. *Acta Crystallogr. A.* **2015**, *71*, 3–8.

(53) Sheldrick, G. M. Crystal Structure Refinement with SHELXL. *Acta Crystallogr. C Struct. Chem.* **2015**, *71*, 3–8.

(54) Dolomanov, O. V.; Bourhis, L. J.; Gildea, R. J.; Howard, J. A. K.; Puschmann, H. OLEX2: A Complete Structure Solution, Refinement and Analysis Program. *J. Appl. Crystallogr.* **2009**, *42*, 339–341.

(55) Macrae, C. F.; Bruno, I. J.; Chisholm, J. A.; Edgington, P. R.; McCabe, P.; Pidcock, E.; Rodriguez-Monge, L.; Taylor, R.; Van De Streek, J.; Wood, P. A. Mercury CSD 2.0 - New Features for the Visualization and Investigation of Crystal Structures. *J. Appl. Crystallogr.* **2008**, *41*, 466–470.

(56) Zhou, D.; Zhang, M.; Ma, Y.; Mukherjee, S.; Liu, J.; Bian, H. Cationic Effects on the Structural Dynamics of the Metal Ion-Crown Ether Complexes Investigated by Ultrafast Infrared Spectroscopy. *J. Phys Chem. B.* **2021**, *125*, 12797–12805.

(57) Ye, Q.; Wang, H. T.; Zhou, L.; Kong, L. H.; Ye, H. Y.; Fu, D. W.; Zhang, Y. Phase Transition Metal-Crown Ether Coordination Compounds Tuned by Metal Ions. *Dalton Trans.* **2016**, *45*, 1000–1006.

(58) Sinitsyn, V. V. Pressure Effect on Phase Transitions in $MeHAO_4$ Superprotonic Conductors (A = S, Se and Me = NH_4, Rb, Cs). *J. Mater. Chem.* **2010**, *20*, 6226–6234.

(59) Dawson, D. M.; Moran, R. F.; Ashbrook, S. E. An NMR Crystallographic Investigation of the Relationships between the Crystal Structure and 29Si Isotropic Chemical Shift in Silica Zeolites. *J. Phys. Chem. C.* **2017**, *121*, 15198–15210.

(60) Le, T. T.; Santhosh, A.; Bordignon, S.; Chierotti, M. R.; Jerabek, P.; Klassen, T.; Pistidda, C. Experimental and Computational Studies on the Formation of Mixed Amide-Hydride Solid Solutions for CsNH2–CsH System. *Results Eng.* **2023**, *17*, 100895-100906.

(61) Malcolm, L. *Spin Dynamics: Basics of Nuclear Magnetic Resonance*; Wiley, Ed.; **2008**.

(62) Lusi, M. Engineering Crystal Properties through Solid Solutions. *Cryst. Growth Des*. **2018**, *18,* 3704–3712.

(63) D'Agostino, S.; Fornasari, L.; Braga, D. Binary and Ternary Solid Solutions of Ionic Plastic Crystals, and Modulation of Plastic Phase Transitions. *Cryst. Growth Des.* **2019**, *19*, 6266–6273.